

Compared abilities of natural (NR) and synthetic (IR) polyisoprene cis-1,4 to crystallize under strain at high strain rates

Nicolas Candau ^{a,b}, Laurent Chazeau ^{,a,b}, Jean-Marc Chenal ^{a,b}, Catherine Gauthier ^c, Etienne Munch ^c*

^aUniversité de Lyon, CNRS, France

^bMATEIS, INSA-Lyon, CNRS UMR5510, F-69621, France

^cManufacture Française des Pneumatiques Michelin, Centre de technologies, 63040 Clermont Ferrand Cedex 9, France

*Corresponding author: Laurent Chazeau, e-mail: laurent.chazeau@insa-lyon.fr

Keywords: strain induced crystallization, natural rubber, synthetic polyisoprene, in situ WAXS, high strain rates

Abstract

Strain induced crystallization (SIC) of a natural rubber (NR) and a synthetic rubber (IR) with a high amount of cis 1,4 units (98.6%) are studied thanks to in situ wide angle X-rays (WAXS)

experiments at room temperature on a large range of strain rates. During stretching at low strain rate ($4.2 \times 10^{-3} \text{s}^{-1}$), SIC in IR occurs at larger stretching ratio than in NR. As a result, the crystallinity index at a given stretching ratio is lower in IR than in NR, in spite of similar crosslink density of the chains involved in the crystallization in both materials. This lower ability for crystallization in IR is attributed to the presence of branching along its backbone and to its lower stereoregularity. Conversely, dynamic experiments performed at high strain rates ($10^1/10^2 \text{s}^{-1}$) show for both materials a similar ability to crystallize. This unexpected result is confirmed by monotonic tensile tests performed in a large range of strain rates. The reason is thermodynamic: the chains extension plays a predominant role compared to the role of the microstructure defects when strain rate is high, i.e. when the kinetics of the crystallite nucleation forces the crystallization to occur at large stretching ratio. A thermodynamic model enables to qualitatively reproduce the experimental results.

1. Introduction

Natural rubber (NR) and Isoprene rubber (IR) are mainly made up of cis (1,4) polyisoprene. In spite of their very similar chemical composition, results from the literature demonstrate that vulcanized IR exhibits weaker tensile strength and tearing resistance than vulcanized NR ^{1, 2}. Besides, data extracted from in situ WAXS tensile tests indicate that NR and IR also display different ability to crystallize under strain ³⁻⁵. For instance, when tensile tests are performed at slow strain rate (lower than 10^{-2}s^{-1}), the stretching ratio at SIC onset (λ_c) in IR compared to NR increases in amount varying from 0.5 ⁴ to 1 ⁶.

In the literature, this difference in SIC behavior between NR and IR finds several explanations. First, NR contains non-rubber components such as inorganic substances, proteins, phospholipids,

carbohydrates and fatty acids ⁷. They could generate a pseudo end-linked network which is claimed to be the reason of the peculiar ability of uncrosslinked NR to crystallize under strain ^{8,9}. Such explanation is however more controversial concerning vulcanized rubbers. Some authors suggest that this pseudo end-linked network could ease SIC in vulcanized NR by making entanglements as permanent nodes ⁹⁻¹¹, and thus eases the appearance of SIC compared to IR. The effect of non-rubber components on thermal induced crystallization (TIC) has been investigated by Tanaka ⁷. From this study, immiscible stearic acid is found to be the only non-rubber component which exhibits a nucleating agent effect. Contrarily to what observed during TIC, Kohjiya et al. have demonstrated that an addition of stearic acid has almost no influence in NR and IR SIC at room temperature ¹². Some authors rather explain the lower ability of vulcanized IR to crystallize under strain by the presence of microstructural defects ^{1,4,6}. In particular, the lower stereoregularity of the synthetic polyisoprene chains should hinders SIC in IR ^{1,4}.

Anyhow, the explanations proposed so far to explain the difference of SIC in natural rubber and synthetic one are based on analysis of data obtained at relatively slow strain rate. Only few results have been reported on SIC at high strain rate, i.e. in conditions close to those met in applications like pneumatic tire. The experiments reported so far to give access to a comparison of SIC kinetics on NR and IR were performed at a fixed stretching ratio ^{13, 14}. They found that SIC kinetics is faster in NR than in IR, whatever the stretching ratio. Nevertheless, no data exists on cyclic or tensile test at high strain rates. Besides, in spite of a large number of thermodynamic models for strain induced crystallization proposed in the literature ¹⁵⁻¹⁹, none of them focused on the comparative study of SIC in NR and IR.

Thus, the aim of this study is to complete the comparison of SIC in NR and IR (containing 98.6% of cis 1,4 units) thanks to WAXS and mechanical analysis interpreted via a thermodynamic modeling. The paper first recalls the main characteristic of SIC behavior of IR and NR, and presents an original study of the thermal stability of the strain induced crystallites in both materials. The results are explained via a thermodynamic approach proposed in a previous paper ²⁰. Then, a unique data set obtained from monotonic tensile tests performed on 6 decades of strain rates, and to in situ WAXS experiments performed during cyclic tensile test in the frequency domain [2-40Hz] enables to compare the crystallization of NR and IR samples at high strain rates. It shows that, for the highest strain rates tested, NR and IR samples exhibit very similar ability to crystallize. Thanks to the previous thermodynamic approach completed by the one of Hoffman-Lauritzen, an interpretation of these new results is proposed.

2. Materials and methods

2.1. Materials

The samples composition is the following: NR rubber gum (Technically Specified Rubber TSR20) or IR gum provided by Michelin Tire Company, stearic acid (2 phr, i.e. 2 g per 100 g of rubber), ZnO (1.5 phr), 6PPD (3 phr), CBS (1.9 phr) and sulfur (1.2 phr). The material has been processed following the Rauline patent ²¹. First, the gum is introduced in an internal mixer and sheared for 2 min at 60°C. Then, the vulcanization recipe is added and the mix is sheared for 5 min. The material is afterward sheared in an open mill for five minutes at 60°C. Sample sheets are then obtained by hot pressing at 170°C during 13 min. Dumbbell-shaped samples, with a 6 mm gauge length (l_0) and 0.8 mm thickness, are machined. The average network chain density ν was estimated from the swelling ratio in toluene and from the Flory – Rehner equation ²² and

found equal to $1.4 \times 10^{-4} \text{ mol.cm}^{-3}$. This density is tuned so that (i) it promotes the development of strain induced crystallization ²³ and (ii) it is high enough to avoid an inverse yield effect ²⁴. In order to avoid microstructure modification during the different mechanical tests, i.e. an uncontrolled Mullins effect, the samples are stretched four times up to stretching ratio ($\lambda = 7$) higher than the maximum stretching ratio reached during the in situ cyclic tests ($\lambda = 6$).

2.2. Mechanical characterization

The EPLEXOR® 500 N of Gabo Qualimeter society (Ahlden, Germany) is used in order to carry out mechanical characterization at different temperatures. Mechanical tests consist of a monotonic stretching at various strain rates, from $5.6 \times 10^{-5} \text{ s}^{-1}$ to $1.1 \times 10^{-1} \text{ s}^{-1}$ and from the relaxed state up to the maximum stretching ratio $\lambda = 6$. Before each tensile test, a soak time of five minutes guarantees that the desired temperature (from -40°C to 50°C), obtained by air circulation, is homogeneous in the oven. The test carried out at the lowest strain rate is stopped at an early stage (λ around 5) because the time reaches the limitations of the experimental set up. To perform experiments at highest strain rates, ranging from $1.1 \times 10^{-1} \text{ s}^{-1}$ to $2.8 \times 10^1 \text{ s}^{-1}$, mechanical characterization is carried out thanks to an MTS tensile test machine. For all the mechanical tests, the tensile force is converted into nominal stress $\sigma = F/S_0$. Stress is then plotted as a function of the stretching ratio $\lambda = l/l_0$. λ is accurately measured by videoextensometry.

When NR or IR crystallizes, its stress strain curves exhibit a relaxation ²⁵ followed by a stress hardening. This is better visualized by plotting the tangent modulus E_t , defined as the derivative $d\sigma/d\lambda$, as a function of λ . It has been widely shown in literature that the stretching ratio at the beginning of this mechanical relaxation gives a good estimate of the crystallization onset λ_c ^{26,27}. Therefore λ_c will be estimated as the stretching ratio at which $dE_t/d\lambda$ is equal to zero.

2.3. In situ WAXS during slow strain rate cycles

The in situ WAXS experiments are carried out on the D2AM beamline of the European Synchrotron Radiation Facility (ESRF). The X-ray wavelength is 1.54 Å. Tests are performed in a temperature-controlled chamber. The following tests are performed: (i) stretching at a constant strain rate ($4.2 \times 10^{-3} \text{ s}^{-1}$), (ii) heating in the deformed state, (iii) thermal cooling in the deformed state after stretching at high temperature (above room temperature). Cooling rate is measured but not controlled. It can be roughly estimated equal to $2^\circ\text{C} \cdot \text{min}^{-1}$.

The two-dimensional (2D) WAXS patterns are recorded by a CCD camera (Princeton Instrument). The beam size is small enough ($300 \mu\text{m} \times 300 \mu\text{m}$) to avoid superimposition with the scattered signal. The background, (i.e. air scattering and direct beam intensities) is properly measured in absence of any sample. It can then be subtracted to the total intensity scattered in the presence of the rubber sample. The corrected scattering intensity is finally normalized by the thickness and the absorption of the sample. Each scattering pattern is integrated azimuthally. The deconvolution of the curve $I=f(2\theta)$ enables the extraction of the intensity at the peak top and the width at half height of each crystalline peak and the intensity at the peak top of the amorphous phase. The crystallinity index CI is then determined as follows ²⁸:

$$CI = \frac{I_{a0} - I_{a\lambda}}{I_{a0}} \quad (1)$$

where I_{a0} and $I_{a\lambda}$ are the intensity of the amorphous phase at the peak top in the unstretched state and the stretched state, respectively. The average crystallite sizes L_{hkl} (L_{200} , L_{102} and L_{002}) in the direction normal to the (hkl) planes, are estimated from the Scherrer equation:

$$L_{hkl} = \frac{K\lambda_w}{\beta_{1/2}\cos\theta} \quad (2)$$

where λ_w is the wavelength and θ is the Bragg angle. In this study, each crystalline peak is fitted with a Lorentzian function in which the width at half-height is $\beta_{1/2}$. According to the parameters chosen for the fit of the experimental peak, the K value is 0.64²⁹. In order to measure the average crystallite size in the stretching direction L_{002} (c_1), the tensile test machine is tilted by an angle around 10°. L_{002} is found independent on the mechanical loading²⁰. It is found equal to 85 Å and 83 Å for NR and IR samples respectively. Besides, an empiric relationship between the crystallites lateral sizes has been established²⁰: $b_1 \sim a_1/3$ with $L_{200} = a_1$ and $L_{020} = b_1$. It must be noted that such relationship has already been found in many other studies^{3,6,23}. The b_1 value is deduced from the measurement of L_{120} . The angle between the plans (120) and (020) being equal to 19°, b_1 (L_{020}) is equal to $0.94L_{120}$. Given the assumption of a parallelepipedic shape for the crystallites, the average volume of the crystallites is then defined by $V = 0.94L_{120}L_{200}L_{002}$ and is therefore proportional to L_{200}^2 .

2.4. In situ WAXS in dynamic conditions

The in situ WAXS experiments are carried out on the DiffAbs beamline of the synchrotron SOLEIL (Gif-Sur-Yvette, France). A specifically dedicated apparatus is developed in order to perform WAXS measurements during cyclic tensile tests with large amplitude and high frequencies (up to 80 Hz)^{30,31}. Thanks to a stroboscopic acquisition, the diffraction pattern is not averaged over the whole cycle, but is acquired at a chosen stretching ratio. In addition, the temperature increase of the material, which can be significant at high frequencies and large amplitude, is also estimated during the test thanks to the measurement of the sample surface

temperature with an Infra-Red pyrometer (CTLF-CF3-C3 of Microepsilon, Saint Germain en Laye, France).

The stroboscopic acquisition of the WAXS pattern at the chosen stretching ratio is made so that the exposure time is $1/44^{\text{th}}$ of the time for a complete cycle. This means that a 1s exposure time at given elongation needs an acquisition over 44 cycles. The device enables to dynamically stretch the samples over a fixed amplitude $\Delta\lambda = \lambda_{\text{max}} - \lambda_{\text{min}}$ ranging from 0 to several hundred percent, around an average pre-stretch λ_a fixed at the beginning of the experiment. The testing procedure is the following: first, the sample is stretched (in 1 s) at a fixed pre-stretch λ_a NR sample is then dynamically deformed around λ_a with the total amplitude $\Delta\lambda$ with an increasing frequency (from 2Hz to 80Hz). Once this sequence is finished, the sample is kept at λ_a during five minutes. During this relaxation phase, the aperture of the stroboscopic system is changed for another position. This procedure is repeated for 8 positions of the cycle, allowing measuring the crystalline parameters during the whole cycle (figure 1).

3. Results and discussion

3.1. Thermal stability of strain induced crystallites in natural and synthetic rubber

Figure 1a recalls the CI evolution of NR and IR samples during a mechanical cycle performed at room temperature and slow strain rate ($4.2 \times 10^{-3} \text{ s}^{-1}$). During the loading, SIC appears at $\lambda_c = 4.3$ (5.1) and totally disappears at $\lambda_m = 3$ (3.6) for NR (IR) sample, leading to an hysteresis curve, as reported in literature ^{3,6,20,23}. The difference between the crystallization curve and the melting one (assumed to be characteristic of the equilibrium state) is explained by the fact that nucleation is a kinetic process involving an energy barrier related to the surface energy of the crystallites. Compared to NR, the melting and crystallization curves of IR are shifted to larger stretching

ratios, whereas the value $\lambda_m - \lambda_c$, related to a so-called “superstraining” effect ²⁰, is not significantly changed, which is consistent with the experimental data of Trabelsi et al. ⁶

NR and IR samples are now stretched up to $\lambda = 6$ at slow strain rate, at sufficiently high temperature to avoid any crystallization during the loading phase. The samples are then cooled down to room temperature while stretching ratio is maintained at $\lambda = 6$. Note that the time scale of cooling is close to the one of the previous stretching experiment performed at room temperature. Crystallization starts at around 80°C and at 60°C for NR and IR respectively. Thus, at a given stretching ratio, IR sample needs to be more cooled to crystallize as compared to the NR sample. A second set of samples is stretched at room temperature and slow strain rate, relaxed during 5 minutes and heated from room temperature up to the temperature of complete melting of crystallites T_m . CI is plotted as a function of the temperature in figure 1b. NR completely melts at T_m around 110°C while IR melts at 90°C. Again, at a given temperature and stretching ratio, CI is always higher in NR than in IR, which is consistent with the studies of Gent ¹ and Trabelsi ⁶.

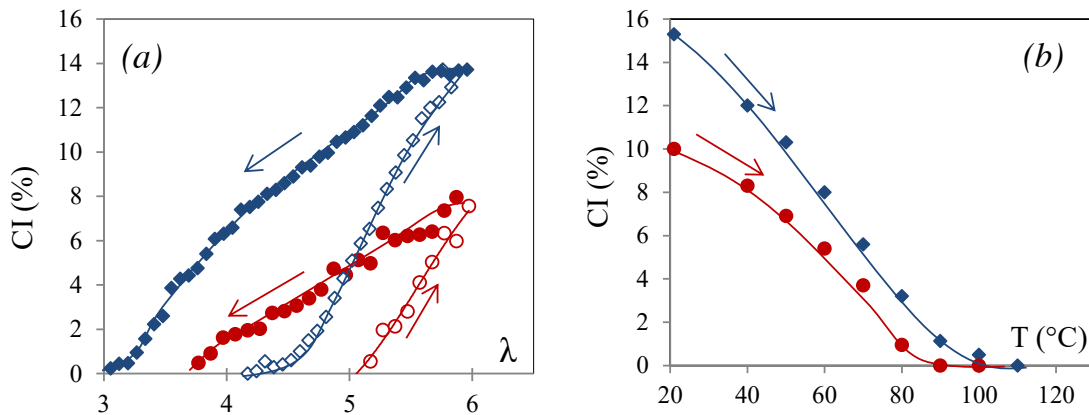


Figure 1. CI during cycle at $4.2 \times 10^{-3} \text{ s}^{-1}$ and at room temperature (a) during heating at $\lambda = 6$ (b) for NR (diamond symbols) and IR (circle symbols) samples. Lines are guides for the eyes.

To more accurately study the thermal stability of strain induced crystallites in NR and IR samples, the evolution of the average size L_{200} in the direction of the a_1 axis of the crystal lattice is depicted in figure 2 as a function of CI for the different tests presented above. The first crystallite sizes we can accurately measure are 45 Å for IR and 50 Å for NR (corresponding to a CI around 0.5%). Then, when CI increases, L_{200} increases and reaches a maximum of 72 Å for IR and 86 Å for NR. One must note that the increase of crystallite size with stretching ratio is not systematically observed in the literature, which should be due to the different methodologies of WAXS analysis used by the others authors. Our methodology was detailed and discussed in a previous paper ²⁰. Anyhow, for a given CI value, similar crystallite sizes between NR and IR samples are measured (only slightly lower for IR), which is consistent with the literature ⁶. For each sample, the relation between L_{200} and CI follows a unique trend whatever the loading or unloading phase. Note that very similar trends are observed concerning melting in the deformed state (figure 2b). Thus, the main difference between NR and IR is a shift of λ_c and λ_m while the difference in crystallites size for a given CI is weak.

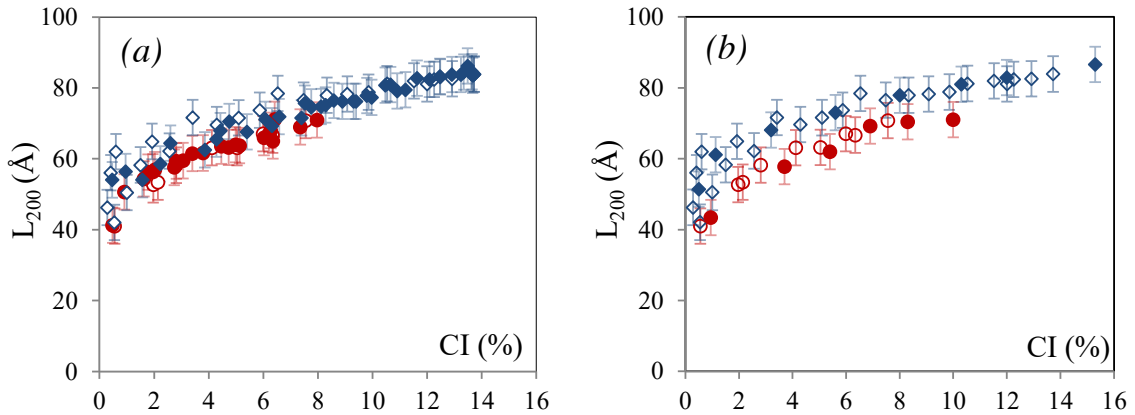


Figure 2. (a) L_{200} versus CI during loading (unfilled symbols) and unloading (filled symbols) at $4.2 \times 10^{-3} \text{ s}^{-1}$ and at room temperature. (b) L_{200} versus CI during loading at $4.2 \times 10^{-3} \text{ s}^{-1}$ and at

room temperature (unfilled symbols) and during heating at $\lambda = 6$ (filled symbols). Circle and diamond symbols are for IR and NR data respectively.

The classical theory of phase transition ³² can be used to interpret the combined effect of crystallites size and stretching ratio on melting temperature (i.e. on thermal stability of crystallites). As proposed in a previous paper ²⁰, from the evolution of the average number of crystallites during SIC, crystallization would be the result of successive appearance of crystallites of increasing size. Once nucleated, one can also assume that the crystallites grow spontaneously – compared to the time scale of the experiment – up to their saturation size in all the directions ($a_1 = a_{\text{sat}}$ and $b_1 = b_{\text{sat}} \sim a_{\text{sat}}/3$ ref. 20, and $c_1 = c_{\text{sat}}$). The melting curve would be the consequence of the successive disappearance of crystallites in the reverse order. Thus, the crystallite dimensions measured at λ close to λ_m correspond to the ones of the most stable crystallites. These crystallites are also the first to appear at λ_c . Assuming an affine deformation of chains, as proposed by Krigbaum et al. ³³, one can write the temperature of total melting T_m , as a function of the total melting stretching ratio λ_m and the dimensions of the last crystallite which melts ³⁴:

$$T_m = \frac{T_{m,\infty} \left(1 - \frac{1}{\Delta H_m} \left(\frac{8\sigma_l}{a_{\text{sat}}} + \frac{2\sigma_e}{c_{\text{sat}}} \right) \right)}{1 - \frac{v_{\text{local}} R T_{m,\infty}}{2\Delta H_m} \left(\lambda_m^2 + \frac{2}{\lambda_m} - 3 \right)} \quad (3)$$

The melting enthalpy ΔH_m (equal to $6.1 \times 10^7 \text{ J.m}^{-3}$ ³⁵) is assumed similar between NR and IR samples since it is expected a same crystalline structure between both materials. For the same reasons, same lateral and chain end surface energies are expected ($\sigma_e = 0.66 \times 10^{-2} \text{ Jm}^{-2}$ and $\sigma_l = 0.33 \times 10^{-2} \text{ Jm}^{-2}$). Their values are deduced from the Thomas-Staveley relationship ³⁶ and from

the assumption that σ_e is almost equal to twice σ_i as proposed in a previous work²⁰. R (8.314 J.mol⁻¹.K⁻¹) is the molar constant gas and v_{local} is the local network density (in mol.cm⁻³) of the chains involved in the most stable crystallites (i.e. the last to melt and the first to crystallize).

According to the literature, the difference in strain induced crystallization (SIC) behavior between vulcanized NR and IR is often attributed to lower stereoregularity of the IR^{6,13,14}. Following the theory of the melting point depression proposed by Flory³⁷ (refer to the formula 12 in the appendix), the stereoregularity defects in IR (~1,4%) can explain an equilibrium melting temperature ($T_{m,\infty}$) around 3°C lower than the one of NR. In synthetic IR, depending on its synthesis, small branching along the polyisoprene backbone could exist (not in the case of NR³⁸⁻⁴⁰) and also cause a decrease of the IR equilibrium melting temperature. Only the paper of Kawahara et al.⁴¹ proposed an estimate of the equilibrium melting temperature of both IR and NR (Differential Scanning Calorimetry was performed on rubbers in 1 wt% hexane solution at different temperatures of crystallization and $T_{md,\infty}$, the equilibrium melting temperature of rubber in diluted state, was deduced from the Hoffman-Weeks plot⁴²). However, the same author did not take into account the dilution effect on $T_{md,\infty}$ to evaluate the $T_{m,\infty}$ (the equilibrium melting temperature of rubber in bulk state). As explained in figure 10 in the appendix, using the data of this study and by applying the necessary correction, we found $T_{m,\infty}$ equal to 33°C for NR and 26°C for IR, i.e a gap of 7°C between both materials attributed both, to the lower stereoregularity (corresponding to a gap of around 3°C) and branching of IR. The $T_{m,\infty}$ of NR is remarkably close to the value (35,5°C) found by Dalal et al.⁴³ thanks to an optical 'turbidimetric' technique applied on bulk NR. Given this value 35.5°C and the gap previously found, $T_{m,\infty}$ should therefore be equal to 28,5°C for IR sample.

From the tensile tests at room temperature, we previously found that $\lambda_m = 3$ and $\lambda_m = 3.6$ for NR and IR respectively, and the size $a_{\text{sat}} (L_{200})$ of the incipient structure. For a CI equal to 0.5 %, the sizes we can accurately measure is 50 Å and 45 Å, for NR and IR respectively. From equation 3 applied at room temperature, we can therefore deduce the network chain densities ν_{local} involved in the formation of the incipient crystallites: it is found equal to $4.1 \times 10^{-4} \text{ mol.cm}^{-3}$ for both samples. These values are around three times higher than the average network chain density measured by swelling (around $1.4 \times 10^{-4} \text{ mol.cm}^{-3}$ for both materials). This is expected, considering the network chain density heterogeneity in both NR and IR samples ⁴⁴⁻⁴⁷. This is also consistent with the general viewpoint which assumes that short chains are the first to orient and consequently the first involved in SIC ^{48,49}. The fact that very similar network chain densities are found for both materials supports that the difference between SIC onset in IR and NR is mainly due to a difference of equilibrium melting temperatures.

Now that the above parameters are estimated, equation 3 provides a relationship between the temperature and the stretching ratio at total melting for IR and NR. It is plotted on figure 3 and compared to the experimental data deduced from the previous loading-unloading curves reported in a previous paper ²⁰: two samples are stretched at room temperature up to $\lambda = 4.3$ and 5.3 respectively and melted at a fixed stretching ratio. The obtained melting couples (λ_m, T_m) are (4.3, 55°C) and (5.3, 80°C) respectively. Predictions and experimental data are in good agreement. In particular, the difference between the total melting temperature of NR and IR is found independent on the stretching ratio. This is consistent with previous experimental results ^{1, 6}. Thus, the depression of the equilibrium melting temperature (around 7°C) due to microstructural defects well explains the lower thermal stability of strain-induced crystallites in IR sample. This should also explain (qualitatively at this stage) why SIC occurs at larger λ_c for

IR, in tensile test experiment at slow strain rate. We shall see in the next section that this difference of λ_c decreases at large strain rate.

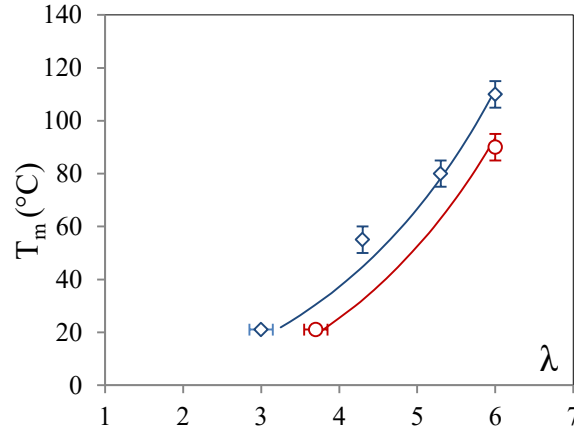


Figure 3. Melting temperature of NR (diamond symbols) and IR (circle symbols) versus the stretching ratio estimated from WAXS experiments in ref. 20. The lines are calculated from equation 3.

3.2. SIC kinetics in natural and synthetic rubbers

As a first approach, a mechanical study is proposed. Samples of NR and IR are stretched over a large strain rate range (from $v_1=5.6 \times 10^{-5} \text{ s}^{-1}$ to $v_3=2.8 \times 10^1 \text{ s}^{-1}$) and temperature range (-40°C to 50°C). Tangent modulus-strain curves ($E_t - \lambda$) for some of the strain rates tested at room temperature are shown in figure 4. The corresponding stress-strain curves $\sigma - \lambda$ are given in insert. Relaxation and hardening, which are typical for SIC (cf. section 2.2), occur at increasing stretching ratio when the strain rate increases.

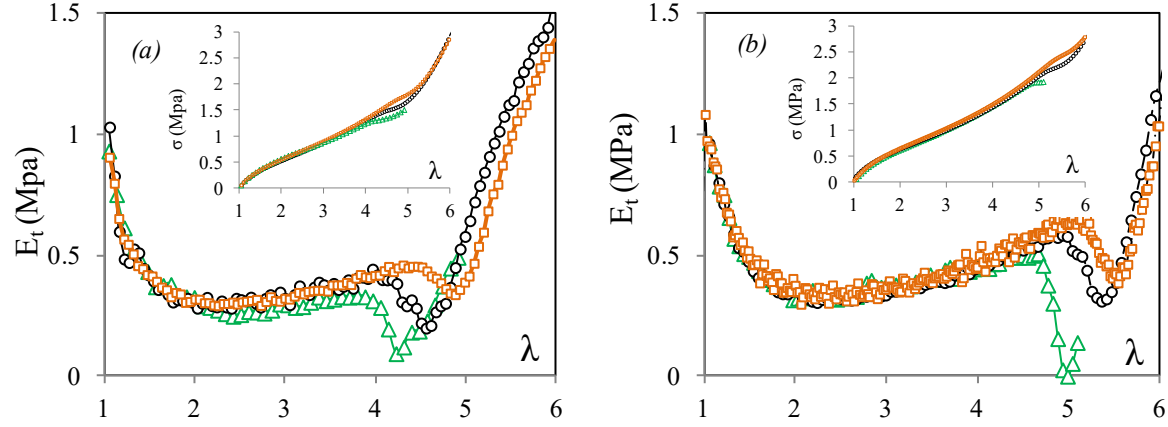


Figure 4. Tangent modulus versus the stretching ratio for NR (a) and IR (b) stretched with the strain rates $v_1 = 5.6 \times 10^{-4} \text{ s}^{-1}$ (triangle symbols), $v_2 = 4.2 \times 10^{-3} \text{ s}^{-1}$ (circle symbols) and $v_3 = 2.8 \times 10^{-2} \text{ s}^{-1}$ (square symbols). The stress-strain curves are given in insert.

The deduced evolution of λ_c (defined as the stretching ratio at which $dE/d\lambda$ is equal to zero) is plotted as a function of the temperature in figure 5a for the strain rate v_2 . For both NR and IR, the optimum temperature for SIC is around -12°C . Indeed, λ_c first decreases when temperature increases from -40°C to around -12°C , and then increases from -12°C to 50°C . The existence of this optimum is explained by the antagonistic effects of an easier chains diffusion at high temperature, and of an easier nucleus formation at low temperature. The value of -12°C for the strain rate v_2 is consistent with the literature. Indeed, in a previous paper⁵⁰ we have found that the optimum temperature for SIC of NR is around -25°C (like for thermal crystallization⁵¹) for slow strain rates (i.e. 10^{-4} s^{-1} and below), and then increases by increasing the strain rate. Similar results have been found on a synthetic rubber¹⁶. It is noteworthy that, above the optimum temperature, λ_c increases with temperature more rapidly with NR than with IR so that their curves seem to converge.

λ_c at room temperature is now plotted in figure 5b as a function of the stretching time corresponding to different strain rates tested. This stretching time corresponds to the time needed to reach the stretching ratio at SIC onset (calculated as the ratio of (λ_c-1) by $\dot{\lambda}$). Data deduced from in situ WAXS experiments (figure 1) are also reported on the same figure, and are found in good agreement with the data deduced from mechanical tests. For the lowest strain rate, λ_c of IR sample is 0.8 above λ_c of NR sample. However, by increasing the strain rate, λ_c significantly increases, more drastically in NR than in IR. Thus, their curves seem to converge.

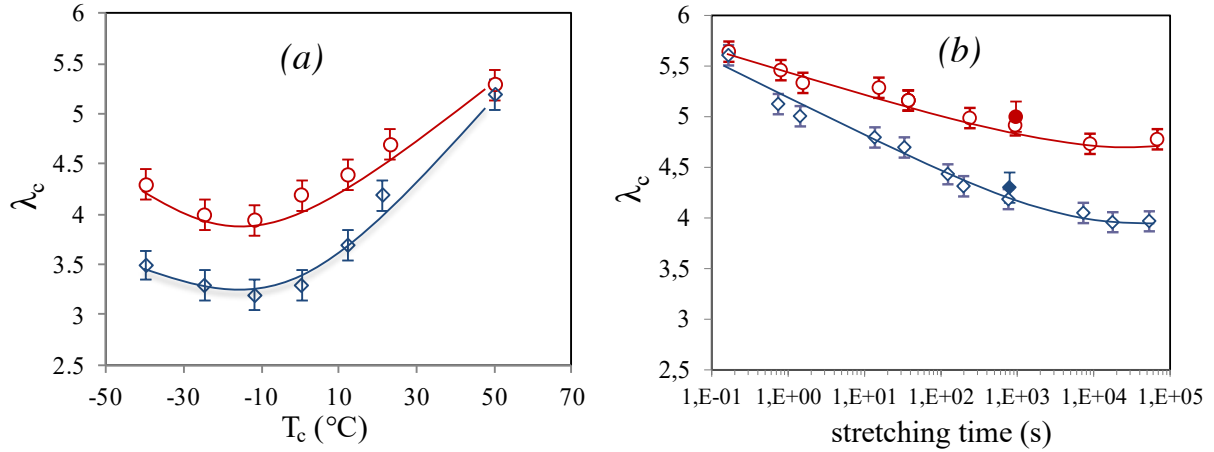


Figure 5. (a) λ_c versus T_c for samples stretched with the strain rate v_2 and (b) λ_c versus the stretching time for samples stretched at room temperature. Values from the mechanical tests are presented with unfilled diamond symbols for NR and unfilled circle symbols for IR. λ_c estimated from WAXS measurements at room temperature (close symbols) are also added (refer to figure 1a). Lines are guides for the eyes.

According to the theory of phase transition ³², crystallization kinetics depends on the nucleation barrier which needs to be crossed. Because only λ_c is considered here, the energetic formalism for primary nucleation is used (in this description, all faces are free to grow as no foreign nucleus

is pre-existent). Following the theoretical developments of reference 20, the free energy of crystallization $\Delta\phi$ can be expressed as a function of the dimension of the crystallite a_1 :

$$\Delta\phi = 2c_1(a_1 + b_1)\sigma + 2a_1b_1\sigma_e - a_1b_1c_1\Delta G_m(T, \lambda) \quad (4)$$

Where c_1 , a_1 and b_1 are the sizes of the crystallites in the directions (002), (200) and (020) and ΔG_m the melting Gibbs free energy which depends on both entropic and enthalpic contributions:

$$\Delta G_m = \Delta H_m \frac{T_{m,\infty} - T}{T_{m,\infty}} + \frac{v_{local}RT}{2} \left(\lambda^2 + \frac{2}{\lambda} - 3 \right) \quad (5)$$

the nucleation barrier $\Delta\phi^*$ can then be written ^{20, 50}:

$$\Delta\phi^* = \frac{32\sigma_l^2\sigma_e}{\Delta G_m^2} \quad (6)$$

For fixed stretching ratio and temperature, the higher is the value of the nucleation barrier energy, the longer is the time needed to allow nucleation. Obviously, nucleation barrier decreases by increasing the stretching ratio, i.e. the strain energy. The lower nucleation barrier energy in NR compared to IR means that crystallization occurs faster in NR sample. From the present description, this is due to the higher melting temperature of the infinite crystal in NR compared to IR.

A nucleation probability, namely N_1 , can be estimated with a Boltzmann's type equation:

$$N_1 = \exp\left(\frac{-\Delta\phi^*}{k_B T}\right)$$

(7)

k_B is the Boltzmann constant. The crystallization rate is then defined as follows ^{16,50}:

$$\dot{N} = \dot{N}_0 D_1 N_1 \quad (8)$$

Where \dot{N}_0 is approximated as a constant (although it should depend on $1/T$), D_1 is a diffusion (or transport) term derived from WLF equation.⁵² This empirical relationship allows estimating the dependence of the relaxation time with temperature, when this one is above the glass transition temperature T_g . D_1 can be written:

$$D_1 = \exp\left(\frac{-2.303C_1C_2}{C_2 + T - T_g}\right) \quad (9)$$

Actually, the diffusion term is not equal but proportional to the exponential term. This coefficient is included in the global pre-factor \dot{N}_0 . Using the time-temperature superposition principle, the shift factor a_T – calculated from the construction of a master curve from mechanical spectrometry data – allows estimating the parameters C_1 , C_2 and T_g , that we found equal to 16.8, 33.6 K and 208 K (-65 °C) respectively, in both NR and IR samples. Note that these parameters were deduced from experiments in the linear regime, i.e. at small strain: we will assume here that the segmental mobility is independent on the stretching ratio ⁵³. The induction time τ needed to observe crystallization can then be roughly estimated from \dot{N} and K (a constant proportional to $1/\dot{N}_0$):

$$\tau = K/(D_1 N_1)$$

(10)

As previously discussed, a difference of the induction times of NR and IR is thought to be due to microstructure defects. In the present description, these defects are taken into account in the term N_1 through the $T_{m,\infty}$ value, which is different for NR and IR. For sake of simplicity, in the following discussion, τ will be approximated as the time needed to reach the stretching ratio at SIC onset, during a monotonic experiment at a fixed temperature. In order to fix the time scale of the theoretical curves and enable their comparison with the experimental trends, we arbitrarily choose to estimate K , an unknown parameter, from the experimental time τ needed to crystallize the NR and IR samples stretched at the optimum temperature (-25°C) with the lowest strain rate tested ($5.6 \times 10^{-5}\text{s}^{-1}$), i.e. when λ_c is the lowest. In these conditions, the time needed to observe crystallization of vulcanised NR (deduced from mechanical response) is around 6300 s and is 3 times higher for IR. Remarkably, K of NR and IR are found very close. The table given in appendix provides the intermediate calculation steps leading to the estimate of K .

From the previous equations and with these fixed parameters, the theoretical value of the stretching ratio at SIC onset can be evaluated for any given temperature and stretching times. Figure 6a displays the evolution of λ_c as a function of the temperature for the strain rate $4.2 \times 10^{-3}\text{s}^{-1}$. As observed experimentally (figure 5a), when varying the temperature, the stretching ratio at SIC onset shows a minimum value corresponding to the fastest kinetics of crystallization. For the highest temperatures, stretching ratio at SIC onset in NR and IR get closer, which is consistent with experimental results. Figure 6b presents the evolution of λ_c as a function of the stretching time at room temperature. Again, curves exhibit trends very similar to the experimental results (figure 5b). In particular, the difference between the stretching ratio at SIC onsets of NR and the one of IR decreases when the strain rate increases (when the stretching time decreases), i.e. when

λ_{cIR} and λ_{cNR} increases. This can be directly demonstrated by the calculation of $\lambda_{cIR} - \lambda_{cNR}$ which writes:

$$\lambda_{cIR} - \lambda_{cNR} = \frac{2\Delta H_m \left(-\frac{T_{m,\infty IR} - T}{T_{m,\infty IR}} + \frac{T_{m,\infty NR} - T}{T_{m,\infty NR}} \right)}{\nu_{local} RT \left(\lambda_{cIR} + \lambda_{cNR} - \frac{2}{\lambda_{cIR} \lambda_{cNR}} \right)} \quad (11)$$

At T constant, this difference decreases with the increase in both λ_{cIR} and λ_{cNR} with the strain rate. Qualitatively, when SIC is forced to occur at higher stretching ratios because of a higher temperature or strain rate, the strain energy term becomes more and more important compared to the enthalpic term (see equation 5). The dependence of this strain energy term with λ^2 being the same for NR and IR, (since their value of ν_{local} are similar), large strain rate tend to attenuate the influence on the nucleation rate of their difference of enthalpic energy, and thus to hinder the effect of the microstructure defects in IR.

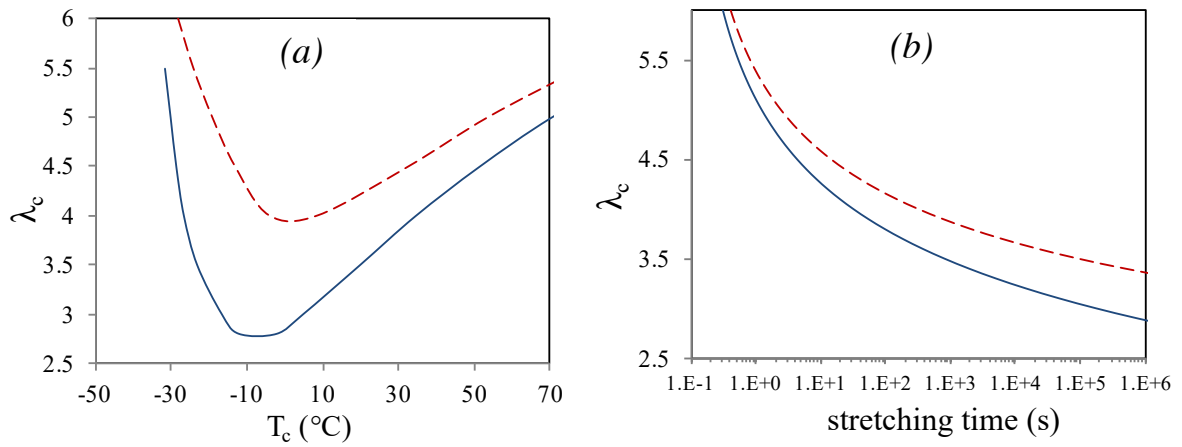


Figure 6. (a) λ_c in NR (solid line) and IR sample (dotted line) for the strain rate $v_2 = 4.2 \times 10^{-3} \text{ s}^{-1}$ versus temperature. (b) λ_c at room temperature versus stretching time for NR (solid line) and IR sample (dotted line).

3.3. Crystallization and melting during high strain rate cycles

The usual conditions of solicitation of natural and synthetic rubbers are more complex than those presented above or in the literature. Thus, our aim is now to understand if the previous experimental observations as well as the thermodynamic developments are still valid when rubber samples are submitted to more complex conditions of solicitations (such as the ones met in pneumatic tires). NR and IR samples are first pre-stretched at $\lambda_a = 4.8$, relaxed during five minutes and then dynamically deformed around λ_a with an amplitude $\Delta\lambda = \lambda_{\max} - \lambda_{\min} = 1.8$ and frequencies varying from 2Hz to 40Hz (cf. section 2.4). Given the relatively high value of pre-stretching, the dynamic cycles are performed above the melting stretching ratio measured at room temperature $\lambda_{m, \text{Troom}}$ (refer to figure 1a).

In figure 7, cycles at 2 Hz are compared to the ones at slow strain rates (10^{-3} Hz). Given its kinetic nature, SIC should depend on strain rate. In spite of that, the CI values measured at λ_{\max} in NR and IR samples are very similar to the ones measured during loading at slow strain rate (cf. figure 1). Indeed, because the chains have not totally relaxed during partial unloading (this is likely since the material is still stretched), re-nucleation is eased³¹. The similarity of the CI value measured at λ_{\min} for slow strain rate cycle and dynamic cycle at 2Hz, also evidenced on filled natural rubbers⁵⁴, is consistent with the scenario proposed in the previous section: each crystallite population involved in the dynamic cycle nucleates during the loading and completely melts during unloading. Thus, the measured CI at λ_{\min} results from the summation of thermally

stable crystallites which are not involved in the dynamic cycle and cannot disappear as long as the temperature of the test is maintained constant.

Then, by increasing the frequency of the test up to 40Hz, CI progressively decreases in both samples, whatever the stretching ratio, even at λ_{\min} , contrarily to what might be expected.

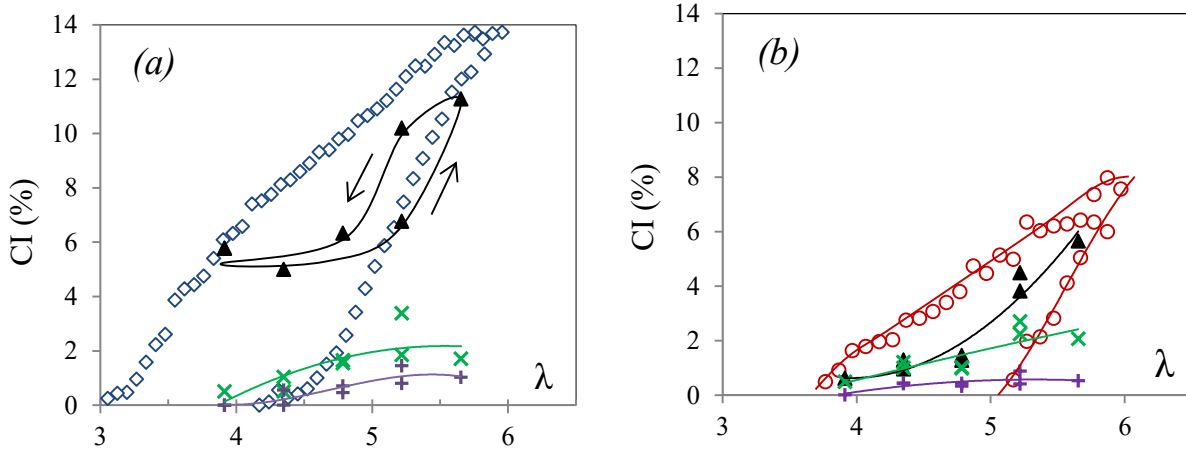


Figure 7. CI versus λ during dynamic tests of NR (a) and IR (b) sample stretched at 2Hz (triangle symbols), 10Hz (cross symbols), and 40Hz (plus symbols). CI curves from the slow strain rate cycles (figure 1) are recalled (diamond symbols and circle symbols for NR and IR samples respectively).

Following the above discussion, the decrease of CI measured at λ_{\min} cannot be due to strain rate effect. As proposed in a previous paper ³¹, the most reasonable explanation is an increase of the materials temperature with frequency, due to self-heating of the sample, which leads to an increase of λ_m . As shown in the insert of figure 8, the temperature surface regularly increases with frequency, similarly in NR and IR, because of their same viscoelastic behavior. CI at λ_{\min} strongly decreases and reaches zero in both samples for frequency above 10-20 Hz. For these frequencies, temperature surface is equal to 33/36°C and 32/36°C for NR and IR samples respectively. Assuming the equivalence between heat brought by self-heating and heat brought

by an external source, the effect of self-heating on the melting stretching ratio can be evaluated from figure 3. At these frequencies, λ_m should be increased up to values equal to 3.8/4 and 4.3/4.4 for NR and IR samples respectively. These values are close or above the λ_{min} values of the dynamic tests (3.9) and thus justify the disappearance of $CI_{\lambda_{min}}$.

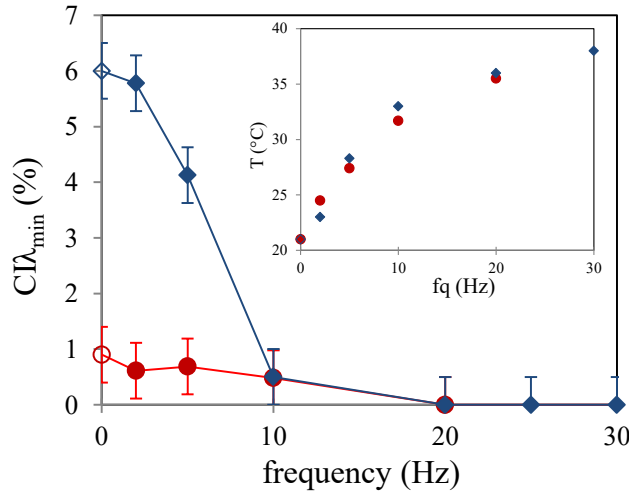


Figure 8. CI at $\lambda_{min} = 3.9$ as a function of frequency for NR (diamond symbols) and IR (circle symbols). CI at $\lambda = 3.9$ measured during the unloading of the slow strain rate cycle is also added (unfilled symbols). In insert: surface temperature of NR (diamond symbols) and IR (circle symbols) samples versus frequency.

The CI evolution at λ_{max} is now plotted as a function of the frequency for IR and NR. CI is higher in NR sample at low frequency. At 10-20Hz and above, $CI_{\lambda_{max}}$ values are equal to the total crystalline fraction (since $CI_{\lambda_{min}}$ is then equal to zero, cf. figure 8) and are found very close for both materials. In these conditions, the first crystallites involved in SIC completely melt during unloading and recrystallize during loading. Thus, SIC characteristic time of the incipient crystallites converge at high frequencies due to the concomitant increase of the self-heating and strain rate. This stays consistent with the previous section 3.2 that showed that an increase of the

temperature (figure 5a), as well as a decrease of the stretching time (figure 5b), tend to bring closer the λ_c of NR and IR samples.

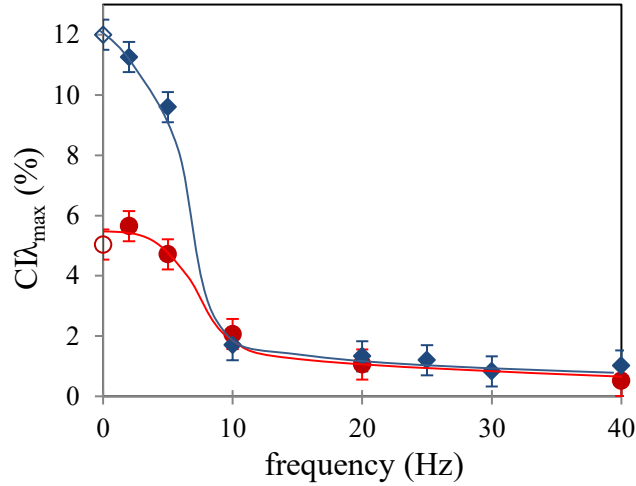


Figure 9. (a) CI at λ_{\max} during dynamic cycles at room temperature in NR (filled diamond symbols) and IR (filled circle symbols) samples. (b) CI during slow stretching at room temperature in NR (unfilled diamond symbols) and IR (unfilled circle symbols) samples.

4. Conclusion

Strain induced crystallization behaviour of natural and synthetic rubbers are compared during monotonic tensile tests with strain rates in the range $[5.6 \times 10^{-5} \text{ s}^{-1} ; 2.8 \times 10^1 \text{ s}^{-1}]$ and during dynamic tensile tests with a corresponding strain rate in the range $[7.2 \text{ s}^{-1} ; 1.44 \times 10^2 \text{ s}^{-1}]$. When stretched at slow strain rate and room temperature, SIC of IR occurs at a larger stretching ratio than NR sample. This is explained by a lower equilibrium melting temperature of IR due to microstructure defects: (i) a lower stereoregularity of chain segments (98.6% of cis 1,4 units for IR against 99.9% for NR) and (ii) the presence of branching along the backbone of the synthetic rubber. Stretching ratios at SIC onset of NR and IR increases and get closer when strain rate or temperature increase. This is explained by the dependence of the different energetic

contributions in the melting free Gibbs energy, on temperature and λ , which actually control the crystallite nucleation. A thermodynamic expression of the nucleation time based on the Hoffman-Lauritzen equation enables to qualitatively describe the experimental results. The convergent ability of NR and IR samples to crystallize at high stretching ratio is confirmed by in situ WAXS experiments performed during dynamic tests at high frequencies (i.e. involving both high strain rates and self-heating). Indeed, these tests show that the crystallinity index measured in both materials at high frequency converge at high strain. In these tests, the effect of the stretching ratio and of the temperature increase are combined since the materials self-heating is significant.

5. Acknowledgements

The authors are indebted to the synchrotron SOLEIL and the local contact Dominique Thiaudière but also the synchrotron ESRF and the local contact Cyrille Rochas for providing the necessary beamline times and technical assistance in the experiments on the DiffAbs line and D2AM line respectively.

6. Appendix

Thermodynamics of polymer melting: following Flory ³⁷, the melting point depression depends on the mole fraction of impurity. Non-crystallizable co-monomers incorporated in the chain are assimilated to impurities, such as monomers in trans configuration. The melting point depression due to their presence is given by:

$$\frac{1}{T_m} - \frac{1}{T_{m,\infty}} = \frac{R}{\Delta H_m} \frac{N_{trans}}{N}$$

(12)

N_{trans} is the number of monomers in trans configuration, N is the total number of monomers in the chain.

In semi-crystalline polymer, the chain-folded lamellar crystals with a thickness L_c show an apparent melting temperature T_m , which depends on the crystallization temperature (T_c). The apparent T_m is always lower than the equilibrium melting temperature $T_{m,\alpha}$ due to the decrease of lamellar thickness. In order to determine $T_{m,\alpha}$, Hoffman and Weeks ⁴² established a method to correlate the melting temperature with the crystallization temperature. Data extracted from the literature (Kawahara et al. ⁴¹) are used to plot figure 10 according to Hoffman-Weeks method. The crystallization measurements of Kawahara et al. were performed on rubbers in 1 wt% hexane solution. Consequently, Hoffman-Weeks plots enable to obtain the equilibrium melting in diluted solution ($T_{md,a}$) for NR (262K / -11°C) and IR (257K / -15°C). The lower equilibrium temperature compared to the ones in dry (bulk) state (for example: 35°C for NR ⁴³) is due to the presence of hexane, a solvent which depresses the melting temperature. A relationship established by Mandelkern et al. ⁵⁵ enables to correct this effect and calculate $T_{m,\alpha}$ from $T_{md,\alpha}$:

$$\frac{1}{T_{md,\alpha}} - \frac{1}{T_{m,\infty}} = \frac{R}{\Delta H_f} \frac{V_u}{V_1} (v_1 - \chi_1 v_1^2) \quad (13)$$

where v_1 represents the volume fraction of solvent, χ_1 ⁵⁶ is the Flory solvent interaction parameter (NR/Hexane), R ⁵⁶ is the molar gas constant, ΔH_f ⁵⁶ is the heat of fusion, V_u ⁵⁶ the molar volume of solvent and V_1 ⁵⁶ the molar volume of the polymer repeat unit.

The $T_{m,\alpha}$ values calculated are 306K / 33°C for NR and 299K / 27°C for IR.

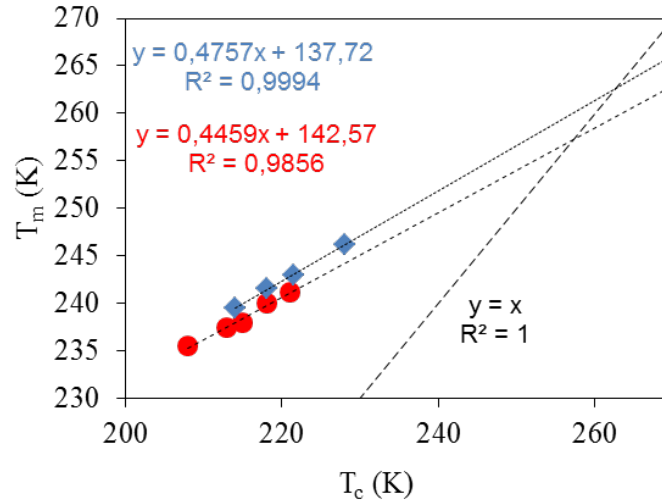


Figure 10. Melting temperature versus crystallization temperature for NR (diamond symbols) and IR (circle symbols) in diluted solution. Data are extracted from Kawahara et al. ⁴¹. Lines correspond to the Hoffman-Weeks plots ⁴².

Sample	λ_c	N_1	D_1	τ (s)	K (s)
NR	1,35	8.89×10^{-3}	2.13×10^{-8}	6.30×10^3	1.19×10^{-6}
IR	2,05	3.43×10^{-3}	2.13×10^{-8}	18.90×10^3	1.38×10^{-6}

Table 1. Steps for the calculations of the constant K. λ_c is the stretching ratio at crystallization onset deduced from tensile tests performed at -25°C with the lowest strain rate ($5.6 \times 10^{-5} \text{ s}^{-1}$). τ is the experimental time needed to reach λ_c . The parameters N_1 and D_1 are the values of the diffusion and nucleation terms deduced from equations 7 and 9 respectively and calculated with $T_c = -25^\circ\text{C}$ and λ_c given in the table. K is finally deduced from equation 10.

7. References

1. A. N. Gent, S. Kawahara and J. Zhao, Rubber Chem. Technol. **71** (4), 668-678 (1998).
2. R. Clamroth and T. Kempermann, Polymer testing. **6** (1), 3-35 (1986).

3. M. Tosaka, D. Kawakami, K. Senoo, S. Kohjiya, Y. Ikeda, S. Toki and B. S. Hsiao, *Macromolecules*. **39** (15), 5100-5105 (2006).
4. M. Tosaka, S. Kohjiya, S. Murakami, S. Poompradub, Y. Ikeda, S. Toki, I. Sics and B. S. Hsiao, *Rubber Chem. Technol.* **77** (4), 711-723 (2004).
5. Y. Shimomura, J. L. White and J. E. Spruiell, *J. Appl. Polym. Sci.* **27** (9), 3553-3567 (1982).
6. S. Trabelsi, P. A. Albouy and J. Rault, *Rubber Chem. Technol.* **77** (2), 303-316 (2004).
7. Y. Tanaka. *Rubber Chem. Technol.* **74** (3), 355-375 (2001).
8. S. Amnuaypornsrri, S. Kawahara, S. Toki, B. S Hsiao, M. Hikosaka, J. Sakdapipanich and Y. Tanaka, *KGK. Kautschuk, Gummi, Kunststoffe*, **65** (6), 46-50 (2012).
9. S. Amnuaypornsrri, S. Toki, B. S. Hsiao and J. Sakdapipanich, *Polymer* **53** (15), 3325-3330 (2012).
10. J. Che, C. Burger, S. Toki, L. Rong, B. S. Hsiao, S. Amnuaypornsrri, A. Nimpai boon and J. Sakdapipanich, *Macromolecules* **46** (11), 4520-4528 (2013).
11. S. Toki, J. Che, L. Rong, B. S. Hsiao, S. Amnuaypornsrri, A. Nimpai boon and J. Sakdapipanich, *Macromolecules* **46** (13), 5238-5248 (2013).
12. S. Kohjiya, M. Tosaka, F. Masahiro, Y. Ikeda, S. Toki and B. S. Hsiao, *Polymer* **48** (13), 3801-3808 (2007).
13. M. Tosaka, K. Senoo, K. Sato, M. Noda and N. Ohta, *Polymer* **53** (3), 864-872 (2012).
13. K. Bruning, K. Schneider, S. V. Roth and G. Heinrich, *Macromolecules* **45** (19), 7914-7919 (2012).
14. M. Tosaka, M., K. Senoo, K. Sato, M. Noda and N. Ohta, N, *Polymer*, **53** (3), 864-872 (2012).

15. P.J. Flory. The Journal of Chemical Physics **15** (6), 397-408 (1947).
16. Y. Miyamoto, H. Yamao and K. Sekimoto, Macromolecules **36** (17), 6462-6471 (2003).
17. M. Tosaka. Macromolecules, **42** (16), 6166-6174 (2009).
18. K. Brüning, K. Schneider, S.V. Roth and G Heinrich, Polymer, **72**, 52-58 (2015).
19. A. Gros, M. Tosaka, B. Huneau, E. Verron, S. Poompradub and K. Senoo, Polymer, **76**, 230-236 (2015).
20. N. Candau, R. Laghmach, L. Chazeau, J.-M. Chenal, C. Gauthier, T. Biben and E. Munch, Macromolecules **47** (16), 5815-5824 (2014).
21. Rauline R. US. Patent, 5, 227, 425, (Michelin) (1993).
22. P. J. Flory and J. Rehner, J. Chem. Phys. **11** (11), 521-526 (1943).
23. J. M. Chenal, L. Chazeau, L. Guy, Y. Bomal and C. Gauthier, Polymer **48** (4), 1042-1046 (2007).
24. P. A. Albouy, J. Marchal and J. Rault, Eur. Phys. J. E **17** (3), 247-259 (2005).
25. A. N. Gent, Transactions of the Faraday Society, **50**, 521-533 (1954).
26. J. Marchal, Thesis, Université Paris Sud-Paris XI, France, 2006.
27. S. Toki and B. S. Hsiao, Macromolecules **36** (16), 5915-5917 (2003).
28. G. R. Mitchell, Polymer **25** (11), 1562-1572 (1984).
29. S. Trabelsi, Thesis, Paris 11, Orsay, France, 2002.
30. N. Candau, L. Chazeau, J. M. Chenal, C. Gauthier, J. Ferreira, E. Munch and C. Rochas, Polymer **53** (13), 2540-2543 (2012).
31. N. Candau, L. Chazeau, J. M. Chenal, C. Gauthier, J. Ferreira, E. Munch and D. Thiaudière, Phys. Chem. Chem. Phys (2015). DOI: 10.1039/C5CP00384A
32. L. H. Sperling, *Introduction to physical polymer science*. (Wiley. com, 2005).

33. W. R. Krigbaum and R. J. Roe, *Journal of Polymer Science Part a-General Papers* **2**, 4391-4414 (1964).
34. N. Candau, L. Chazeau, J.-M. Chenal, C. Gauthier, R. Laghmach, T. Biben and E. Munch, *Polymer* **60**, 115-124 (2015). doi:10.1016/j.polymer.2015.01.029
35. H. G. Kim and Mandelkern.L, *Journal of Polymer Science Part A-2-Polymer Physics* **10** (6), 1125-1133 (1972).
36. J. D. Hoffman, Davis, G. T., & Lauritzen Jr, J. I., *Treatise on Solid State Chemistry*. (New York, 1976).
37. Flory and P. J., *Principles of polymer chemistry*. (Cornell University Press, 1953).
38. I.Y. Poddubnyi and E.G. Erenburg, *Rubber Chem and Technol* **36** (3), 807-814 (1963).
39. A. W. Johnson (Jones & Bartlett learning) Chapter 18 : Synthetic polymer p659 (1999).
40. C. Kim, J. Sainte-Beuve, S. Guilbert S and F. Bonfils, *European Polymer Journal* **45** (8), 2249-2259 (2009).
41. S. Kawahara, Y. Inomata, Y. Tanaka and N. Ohya, *Polymer* **38** (16), 4113-4116 (1997).
42. J. D. Hoffman and J. J. Weeks, *J Res Natl Bur Stand A* **66** (1), 13-28 (1962).
43. E. N. Dalal, K. D. Taylor and P. J. Phillips, *Polymer* **24** (12), 1623-1630 (1983).
44. T. Suzuki, N. Osaka, H. Endo, M. Shibayama, Y. Ikeda, H. Asai, N. Higashitani, Y. Kokubo and S. Kohjiya, *Macromolecules* **43** (3), 1556-1563 (2010).
45. Y. Ikeda, N. Higashitani, K. Hijikata, Y. Kokubo, Y. Morita, M. Shibayama, N. Osaka, T. Suzuki, H. Endo and S. Kohjiya, *Macromolecules* **42** (7), 2741-2748 (2009).
46. A. Vieyres, R. Pérez-Aparicio, P.-A. Albouy, O. Sanseau, K. Saalwächter, D. R. Long and P. Sotta, *Macromolecules* **46** (3), 889-899 (2013).

47. J. L. Valentin, P. Posadas, A. Fernandez-Torres, M. A. Malmierca, L. Gonzalez, W. Chasse and K. Saalwachter, *Macromolecules* **43** (9), 4210-4222 (2010).
48. M. Tosaka, S. Murakami, S. Poompradub, S. Kohjiya, Y. Ikeda, S. Toki, I. Sics and B. S. Hsiao, *Macromolecules* **37** (9), 3299-3309 (2004).
49. S. Toki, I. Sics, B. S. Hsiao, S. Murakami, M. Tosaka, S. Poompradub, S. Kohjiya and Y. Ikeda, *J. Polym. Sci. Pt. B-Polym. Phys* **42** (6), 956-964 (2004).
50. N. Candau, L. Chazeau, J. M. Chenal, C. Gauthier, R. Laghmach, T. Biben and E. Munch, *European Polymer Journal* **64** 244-252 (2015).
doi:10.1016/j.eurpolymj.2015.01.008
51. J. M. Chenal, L. Chazeau, Y. Bomal and C. Gauthier, *J. Polym. Sci. Pt. B-Polym. Phys* **45** (8), 955-962 (2007).
52. M. L. Williams, R. F. Landel and J. D. Ferry, *Journal of the American Chemical Society* **77** (14), 3701-3707 (1955).
53. E. Munch, J-M. Pelletier, B. Sixou and G. Vigier, *Physical review letters* **97** (20), 207801 (2006).
54. N. Candau, L. Chazeau, J. M. Chenal, C. Gauthier and E. Munch, *Composites Science and Technology* **108**, 9-15 (2015). doi:10.1016/j.compscitech.2014.12.014
55. L. Mandelkern, .R. Garrett and P.J. Flory, *Journal of the American Chemical Society* **74** (15), 3949-3951 (1952).
56. *Polymer data Handbook*, Oxford University Press (1999).